Error Analysis for High Resolution Topography with Bi-static Single-Pass SAR Interferometry

Ronald J. Muellerschoen, Curtis W. Chen, Scott Hensley, Ernesto Rodriguez
Radar Science and Engineering
Jet Propulsion Laboratory
California Institute of Technology
Pasadena, CA, USA, Ronald.J.Muellerschoen@jpl.nasa.gov

Abstract

We present a flow down error analysis from the radar system to topographic height errors for bi-static single pass SAR interferometry for a satellite tandem pair. Because of orbital dynamics the baseline length and baseline orientation evolve spatially and temporally, the height accuracy of the system is modeled as a function of the spacecraft position and ground location. Vector sensitivity equations of height and the planar error components due to metrology, media effects, and radar system errors are derived and evaluated globally for a baseline mission. Included in the model are terrain effects that contribute to layover and shadow and slope effects on height errors. The analysis also accounts for non-overlapping spectra and the non-overlapping bandwidth due to differences between the two platforms' viewing geometries. The model is applied to a 514 km altitude 97.4 degree inclination tandem satellite mission with a 300 m baseline separation and X-band SAR. Results from our model indicate that global DTED level 3 can be achieved.

Spell out

Background

Topographic maps have been computed with spaceborne single-pass SAR interferometry such as the Shuttle Radar Topography Mission (SRTM) [Rosen et al. 2000]. The height accuracy of these Digital Elevation Models (DEMs) is partially restricted due to the physical baseline separation of the two receiving antennas on the single platform. Larger baseline separations are possible with repeat-pass SAR interferometry as has been demonstrated with ERS, JERS, and RADARSAT, but coherence of the interferogram can be reduced due to temporal decorrelation of the scene due to changes in the surface scattering as well as media effects of the ionosphere and troposphere [Zebker et al. 1994, Rosen et al. 2000]. To achieve high-resolution topography, both single pass SAR interferometry and large baseline separations are desirable.

SRTM obtained elevation data on a near-global scale to generate a DTED level 2 (30 meter postings) Digital Elevation Model (DEM). This is currently the most complete high-resolution digital topographic database of the Earth. The German Aerospace Center DLR has proposed to generate a global DEM corresponding to DTED level 3 specification (12 meter postings[1]) by means of a second SAR satellite (TanDEM-X) flying in a tandem orbit configuration with TerraSAR-X [Moreira et al. 2004]. Using the TanDEM-X pair as an initial design, we globally evaluate performance of the tandem orbit configuration as it evolves over time. Error contributions from the individual components change over time due to geometry considerations and we seek to find the time at which the overall height and planimetric InSAR errors are minimal.

Error Sources

The error sources for the DEM model that we consider are: 1.) random and systematic phase noise, 2.) baseline length uncertainty errors, 3.) baseline orientation errors, 4.) platform velocity errors, 5.) wavelength errors which are due to both the local oscillator stability and due to the Prati shift effects, 6.) ranging errors due to timing and media effects of the troposphere and ionosphere, and 7.) absolute platform position errors. These error sources are considered independent in this study. An RSS of the individual error sources produces vertical and planimetric errors for the InSAR configuration.

[1] HRTI Level 3 requirements specify 10-meter postings; DTED Level 3 is less stringent and averages to 12-meter postings. In both specifications for horizontal-circular error at 90% probability (CE90) is 3 meters relative and 10 meters absolute. The vertical-linear error at 90% probability (LE90) is 2 meters relative and 10 meters absolute.

Formulation of Error Sources

The basic reconstruction equation represents the topography $\overline{R}$ as a sum of the platform position $\overline{P}$ and a vector $\rho\hat{n}$ from the platform to the resolution cell, where ρ is the slant range and $\hat{n}$ is the look vector.

$$\overline{R} = \overline{P} + \rho\hat{n} \tag{1}$$

The errors in the interferometric measurement can then be represented by:

$$\delta\overline{R} = \delta\overline{P} + (\delta\rho)\hat{n} + \rho(\delta\hat{n}) \tag{2}$$

The first term maps errors in the platform metrology directly to errors in the topography. The second term originates from system timing and delay errors, and to signal delays due to propagation through an inaccurately modeled medium. System delays can be calibrated by observing known ground control points and are typically stable over data collects. The last term involves measurements of phase, baseline length, baseline orientation, velocity, and the wavelength. Appendix (A9) shows the variation of the look vector with respect to variations in the phase Φ, and the variation in the baseline direction $\hat{b}$, while (A10) shows the variation of the look vector with respect to the variation in the velocity $\hat{v}$.

$$\delta\hat{n} = -\left[\frac{1}{kB}\delta\Phi + \hat{n}\cdot\delta\hat{b}\right]\frac{\hat{n}\times\hat{v}}{\hat{b}\cdot(\hat{n}\times\hat{v})} \tag{3}$$

$$\delta\hat{n} = -\left[\hat{n}\cdot\delta\hat{v}\right]\frac{\hat{n}\times\hat{b}}{\hat{v}\cdot(\hat{n}\times\hat{b})} \tag{4}$$

Using (3) and (2) we can compute then the topographic partial with respect to phase (5).

$$\frac{\delta\overline{R}}{\delta\Phi} = -\frac{\rho}{kB}\frac{\hat{n}\times\hat{v}}{\hat{b}\cdot(\hat{n}\times\hat{v})} \tag{5}$$

The error of $\overline{R}$ in the direction of the vertical is then the partial of the topographic height error with respect to phase (6).

$$\frac{dh}{\delta\Phi} = -\frac{\rho}{kB}\frac{\hat{n}\times\hat{v}}{\hat{b}\cdot(\hat{n}\times\hat{v})}\cdot\hat{h} \tag{6}$$

The errors in the baseline $\delta\hat{b}$ can be expressed as errors in the baseline length and errors in baseline orientation (7).

$$\delta\hat{b} = \frac{\hat{b}}{B}\delta B + \left(\hat{w}\times\hat{b}\right)\delta\Omega \tag{7}$$

Using (7) (3) and (2), we can express the topographic height errors with respect to baseline length errors (8), and with respect to errors in the orientation (9).

$$\frac{dh}{\delta B} = -\frac{\rho\left(\hat{n}\cdot\hat{b}\right)}{B}\frac{\hat{n}\times\hat{v}}{\hat{b}\cdot(\hat{n}\times\hat{v})}\cdot\hat{h} \tag{8}$$

$$\frac{dh}{\delta\Omega} = -\rho\left(\hat{n}\cdot\left(\hat{w}\times\hat{b}\right)\right)\frac{\hat{n}\times\hat{v}}{\hat{b}\cdot(\hat{n}\times\hat{v})}\cdot\hat{h} \tag{9}$$

Assuming the error in the velocity is only of the form (10)

$$\delta\hat{v} = \frac{\hat{v}}{v}\delta v \tag{10}$$

we can combine this with (4) and (2) to obtain the topographic height errors with respect to velocity errors (11).

$$\frac{dh}{\delta v} = -\frac{\rho(\hat{n}\cdot\hat{v})}{v}\frac{\hat{n}\times\hat{b}}{\hat{v}\cdot(\hat{n}\times\hat{b})}\cdot\hat{h} \tag{11}$$

In a similar fashion, the variation of the look vector with respect to the wavelength λ is given by (12).

$$\delta\hat{n} = \frac{\delta\lambda\left[(\hat{n}\cdot\hat{b})\hat{n}\times\hat{v} - (\hat{n}\cdot\hat{v})\hat{n}\times\hat{b}\right]}{\lambda\ \ \hat{b}\cdot(\hat{n}\times\hat{v})} \tag{12}$$

Combining (12) and (2) we obtain the topographic height errors with respect to the wavelength errors.

$$\frac{dh}{\delta\lambda} = \frac{\rho}{\lambda}\frac{\left[(\hat{n}\cdot\hat{b})\hat{n}\times\hat{v} - (\hat{n}\cdot\hat{v})\hat{n}\times\hat{b}\right]}{\hat{b}\cdot(\hat{n}\times\hat{v})}\cdot\hat{h} \tag{13}$$

Phase Noise

The partial of the height error due to phase error is given by (6). A Cramer-Rao bound determines the phase noise standard deviation from the interferometric correlation and the effective number

of looks (14). We assume that geometric, temporal, volumetric, and rotational decorrelations are negligible compared to the thermal-noise correlation γ_{SNR}. That is $\gamma \approx \gamma_{SNR}$ where γ_{SNR} is given by (15).

$$\sigma_{\Phi} = \frac{1}{\sqrt{2N_L}} \frac{\sqrt{1-\gamma^2}}{|\gamma|} \tag{14}$$

$$\gamma_{SNR} = \frac{SNR}{SNR+1} \tag{15}$$

Ambiguous Heights

If the change of the topography as observed by the phase difference of the two receiving antennas is larger than 2π, the reconstructed height change is ambiguous when phase unwrapping. The maximum limit of the ambiguous heights can be expressed as (16) and (17).

$$h_a = 2\pi \left| \frac{dh}{d\Phi} \right| \tag{16}$$

$$\left| \frac{dh}{d\Phi} \right| = \frac{\rho\lambda \sin(i)}{2\pi p B_{\perp}} \tag{17}$$

In (17), we use (6) but for broadside viewing geometry and simplicity we replace equivalent scalars $B\hat{b} \cdot (\hat{n} \times \hat{v})$ with the perpendicular component of the baseline $B_{\perp}$, and $(\hat{n} \times \hat{v}) \cdot \hat{h}$ with sin(i), where i is the incidence angle. Additionally the effective wave-number k was replaced by $2\pi p/\lambda$, where p is either a 1 or 2 depending on whether single-antenna transmit mode or dual-antenna transmit mode (ping-pong).

In this study, one of the constraints imposed on the system is to have better (larger) than 50-meter minimum ambiguous height.

Effective Number of Looks

The effective number of looks N_L in (14) is the output post size per resolution element on the ground $\delta_x \delta_y$. This is additionally scaled to account for the non-overlapping spectra due to different azimuth viewing angle and the non-overlapping bandwidth from the Prati shift due to different incidence angles. Equation (18) shows these relationships.

$$N_L = \frac{\Delta x_{\text{post}} \Delta y_{\text{post}}}{\delta_x \delta_y} \left(1 - \frac{\theta_{\text{azoffset}}}{\theta_{\text{SA}}}\right)\left(1 - \frac{B_{\perp}}{B_{\text{crit}}}\right) \tag{18}$$

In the first scaling, the angular extent of the synthetic aperture spanned by the target point θ_{SA} must be larger than the angular offset in azimuth $\theta_{azoffset}$ between the two images for Doppler spectral overlap. If the azimuth offset is larger than θ_{SA} there is decorrelation, and no interferometry is possible.

In the second scaling, $B_{\perp}$ is the perpendicular component of the interferometric baseline and B_{crit} is the critical baseline (22 below). At the critical baseline there is no overlap in the correlated spectrum and again no interferometry is possible.

Slope Effects

Terrain-slope effects can have a significant impact on the accuracy of height estimates derived from InSAR data. Terrain-induced slopes alter the range-spectral overlap between the two SAR channels comprising the interferogram by reducing the local interferometric coherence. Moreover, layover and shadow can lead to voids in the data where valid height estimates are not possible. Furthermore, significant terrain variations make phase-unwrapping "holes" and/or errors more likely, especially when the ambiguous heights are small. It is therefore important that terrain effects be modeled.

In this study we model the terrain-slope effects as decreasing the correlation coefficient due to a smaller spectral overlap and also fewer looks due to an increase of the range resolution as projected onto the ground as will be explained.

Terrain statistics are difficult to model because land-surface shapes and characteristics vary greatly over the Earth. Moreover, problems arising from layover, shadow, and phase unwrapping are due to non-local phenomena. The terrain at one location can influence height estimates at a different location though these mechanisms. Because terrain effects are important, yet difficult to characterize rigorously, we adopt a heuristic model. While this model makes many approximations, we view it as a starting point for modeling terrain effects. The full derivation of the model is outside the scope of this paper, but the modeling methodology is described as follows.

Suppose that a locally stationary random process can approximate terrain heights with an isotropic 2-D piecewise power-law power spectral density (PSD). The characteristics of power-law spectra therefore imply that the expected height variation over a given horizontal cell depends on the size of the cell and the cell sampling resolution. We examined DEMs from various sources to estimate power-law slope parameters, which are assumed to be constant over the entire Earth. The local terrain statistics are therefore characterized by an overall scale factor on the PSD. We use a low-resolution DEM with global coverage to estimate this scale factor as a function of Earth-surface location.

With the local terrain PSD characterized, we use the piecewise power-law in order to extrapolate the low-resolution, wide-area height variability to the high-resolution measurements desired. The estimated RMS height variability σ_z as determined from the GTOPO30 global digital elevation map (DEM) [edc.usgs.gov/products/elevation/gtopo30/gtopo30.html] is then transformed into a slope-variability parameter θ_{slope} by dividing by the desired high-resolution horizontal posting. While this height-to-slope transformation neglects the fact that SAR data are uniformly sampled in the slant plane rather than the horizontal (ground) plane, it is useful for first-order analyses.

The resolution element on the ground δ_y in computing the effective number of looks N_L in (18) must account for a slant range reduction due to the local slope. Figure 1 shows the geometry.

The radar slant range resolution $\delta\rho$ projected on a flat Earth δy is $\delta\rho/\sin(i)$ where i is the incidence angle from the horizontal (flat-Earth) line to the dotted line in Figure 1. Geometry shows that the projection of the slant range resolution due to the terrain-slope onto flat Earth can be represented by (19).

$$\delta y_{slope} = \frac{\delta p \cos(\theta_{slope})}{\sin(\theta_i - \theta_{slope})} = \frac{\delta y \sin(i)\cos(\theta_{slope})}{\sin(\theta_i - \theta_{slope})} \qquad (19)$$

When considering slope-effects, the effective number of looks N_L in (18) must then include (19), as in (20).

$$N_{L(slopes)} = N_L \frac{\sin(\theta_i - \theta_{slope})}{\sin(i)\cos(\theta_{slope})} \qquad (20)$$

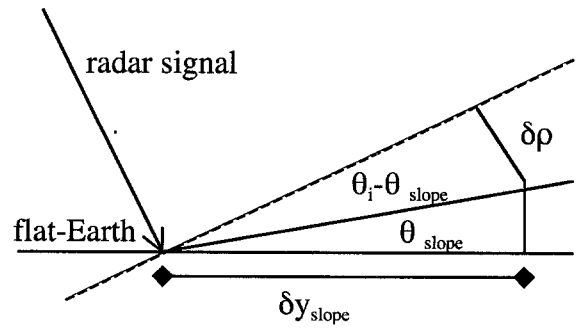

Figure 1. Geometry for slope effects on slant range projection onto flat-Earth.

A secondary effect of terrain-slopes is a reduction of the correlation due to decreased spectral overlap after Prati filtering to a flat surface. That is $\gamma \approx \gamma_{SNR}\gamma_{Geom}$ where γ_{Geom} is given by (21) (22) and (23).

$$\gamma_{Geom} = \frac{1 - \left|\frac{B_\perp}{B_{crit_slope}}\right|}{1 - \left|\frac{B_\perp}{B_{crit}}\right|} \qquad (21)$$

$$B_{crit} = \frac{\lambda\rho\tan(\theta_i)}{p\delta p} \qquad (22)$$

$$B_{crit_slope} = \frac{\lambda\rho\tan(\theta_i - \theta_{slope})}{p\delta p} \qquad (23)$$

Here again p is 1 or 2, and $\delta\rho$ is the slant range resolution. Equation (21) represents the fraction of spectral overlap remaining after Prati filtering to a flat surface for spectral shifts with and without terrain-slope effects.

Finally, the fraction of sampled posts invalidated by layover and shadow effects are computed using a model parameterized in terms of θ_{slope} and θ_i. This parametric model was derived empirically by using SRTM and GeoSAR DEMs to feed geometry-specific simulations of LEO SAR sensors.

Future work will involve the inclusion of similar empirical parametric models for phase-unwrapping errors.

Error Assumptions

For the case study, the orbit height is modeled at 514 km. The radar system parameters at X band model the pulse width at 52 microseconds with 2.26 kW peak power. We also use the DLR model of a 4.8 m x 70 cm antenna aperture. Radar performance models of this system yield a ground swath of 20 km. A ground point moving at 7 km/sec swaps out 140 km^2 /sec for area coverage rates.

The random phase noise (14) is modeled as a function of the number of looks and the SNR values from the radar model as specified in Table 1. Over a span of incidence angles we hold the range resolution on the ground fixed to 3 meters by altering the transmitted bandwidth.

Incidence(deg)	25	30	35	40	45	50
Bandwidth(Mhz)	100	90	78	68	63	60
SNR in swath(dB)	8.6	11.1	10.1	9.4	8.1	7.0

Table 1. Radar model used for study lists the worse case SNR over the swath for increasing incidence angles.

We additionally assume a 10-degree systematic uncertainty in the phase noise. The GPS metrology [Remco, 2005] and mechanical/electrical alignment in an RSS sense yields 1.37 mm of baseline error. The baseline orientation error is modeled as a function of the baseline length error due a simple lever arm effect. The velocity errors are 20.e-6 m/sec and derive from Grace GPS-only overlapping orbit solutions. The wavelength errors are assumed to be 1e-10 meter. The range error due to the timing and media errors is 11.4 cm in an RSS sense; this includes 5 cm for timing, 10 cm for troposphere, and 2 cm for ionosphere. Finally GPS-only solutions in down-track can achieve accuracies at the 10 cm level for absolute position errors.

Results for Orbit Configurations

We evaluate several orbit scenarios to compute the minimum RSS topographic height error as the tandem-orbit evolves over its 11-day repeat track. From the interferometric height sensitivity equations above, to minimize the height errors we need to maximize the interferometric perpendicular component of the baseline between the two platforms. This simplistic notion however has its limitations in that at some point of increasing the baseline length, phase unwrapping errors will affect the performance of the interferogram due to decreasing ambiguous heights. The platform separation we consider in this study is 300 meters.

At each second in the orbits, we evaluate all ground grid points in the potential swath, both left and right looking sides of the radar, and we save only error contributions of the minimum RSS height accuracy. To aid in searching through the nearly 1/2 million 0.2x0.2 degree grid points, we require certain geometric criteria to be met. First the ground elevation angle must be larger than 10 degrees. This quickly reduces the number of points over the globe to a more manageable data set. Second, the look angle must be between 20 and 70 degrees, and the squint angle must be +/- 2 degrees. Additionally, the incidence angle must be from 25 to 50 degrees, the ambiguous heights must be larger than 50 meter, and image time offsets must be less than 0.5 seconds. Also as per (18), the angular offsets must be less than the angle subtended by the synthetic aperture and the perpendicular component of the baseline must be less than the critical baseline. Additional criteria require that the fraction of posts in layover and shadow must be smaller than 10 %.

In the orbit configuration study we are looking for trends to optimize tandem-orbit performance. The first orbit we consider is a simple pendulum type orbit, where the two platforms move back and forth relative to each other once per rev. This can be achieved simply by offsetting the ascending nodes of the two platforms. The eccentricity, inclination, and argument of periapsis are held the same. This results (Figure 2) in horizontal baselines at low latitudes but small baselines at high latitudes.

The second orbit we consider is a cartwheel configuration where the platforms are in the same plane (same ascending nodes) but 180 degrees offset in the argument of periapsis. In this configuration the baseline oscillates between along track and vertical offsets. This results (Figure 3) in large vertical baselines at the poles. The large along-track separation at the low latitudes does not translate into large interferometric baselines since the trailing spacecraft must image the same point on the ground as the leading spacecraft. However due to Earth rotation, there is a component of the baseline that is in the cross-track direction of the image ground point. We can additionally rotate the cartwheel configuration to come up with a third orbit such that the vertical offsets lie along the low latitudes and the along-track offsets are near the poles. We will refer to this as the rotated cartwheel.

The fourth type of orbit we consider is a corkscrew configuration where we offset both the ascending nodes as in the pendulum, and offset the argument of periapsis by 180 degrees as in the cartwheel. This results (Figure 4) in large vertical baselines at the poles as the cartwheel orbit and in large horizontal baselines at low latitudes as the pendulum orbits.

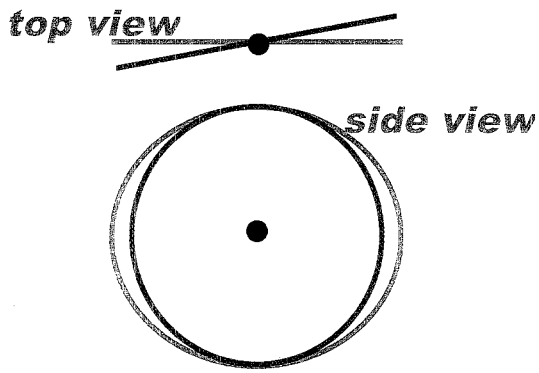

Figure 2. Pendulum type orbit with top view looking down from the pole, and side view looking at the equator shows horizontal baselines at the low latitudes but small baselines at the poles.

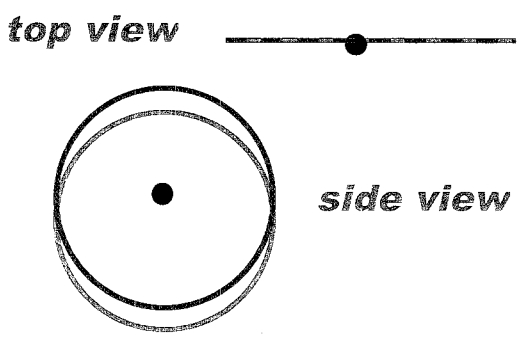

Figure 3. Cartwheel type orbit with top view looking down from the pole, and side view looking at the equator shows vertical offsets in the baseline at the poles. Along track offsets at the equator do not necessarily translate into large interferometric baselines.

Table 2 lists the four tandem-orbit configurations and the associated minimum R.M.S. (root-mean-square) height errors as accumulated over the 11-day repeat orbits. Represented in Figures 5, 6, 7, 8 are the 1-sigma absolute height errors from the minimum heights as RSS'ed from the individual error sources over the 11-day repeat cycle for the different orbit configurations. The scales for Figures 5, 6, 7, 8 are in meters. The pendulum configuration (Figure 5) yields large height errors near the poles where we have a small perpendicular component of the interfereometric baseline, and progressively smaller errors nearer the equator. The cartwheel configuration (Figure 6) yields smaller errors near the poles due to the larger vertical offset of the platforms. Re-phasing this to a rotated cartwheel configuration (Figure 7) yields smaller errors at low latitudes. Finally the corkscrew configuration (Figure 8) produces the largest perpendicular component of the baseline on a global scale; the result is a more uniform distribution of the height errors over the Earth.

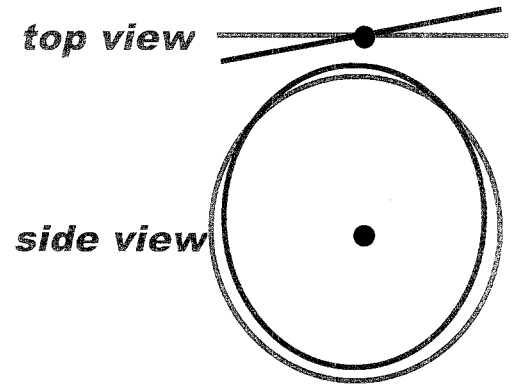

Figure 4. Corkscrew type orbit with top view looking down from the pole, and side view looking at the equator shows vertical baselines at the poles and horizontal baselines at low latitudes.

tandem orbit	R.M.S. (meters)
300 m pendulum	5.15
300 m cartwheel	4.00
300 m rotated cartwheel	3.79
300 m corkscrew	3.00

Table 2: Global R.M.S. of topographic height errors associated with different tandem orbit configurations. Outlier points above 20 meters have been removed from the statistics. The postings are to 12 meters.

The 1/2 million 0.2x0.2 degree sampled grid points are sorted according to absolute height errors and 3 sample points are presented in Table 3. Listed are sample values at 15 %, median, and 85 % of the max height error. The table additionally presents the error contributions from the individual error sources. We assume that only relative phase errors contribute to the relative DEM errors and that the RSS of all the error sources contribute to the absolute error. For DTED Level 3, the relative requirement is 3 m CE90 (horizontal) and 2 m LE90 (vertical). The absolute DTED Level 3 requirement is 10 meters for both CE90 and LE90. The dominant error source to the absolute error in all cases is the baseline length uncertainty.

Slope effects contribute to the relative error budget where there are significant slopes. On a global scale, analysis shows that the R.M.S. for relative height errors (phase only errors) neglecting slope is 1.22 m; when considering slope affects the global R.M.S. is 1.39m.

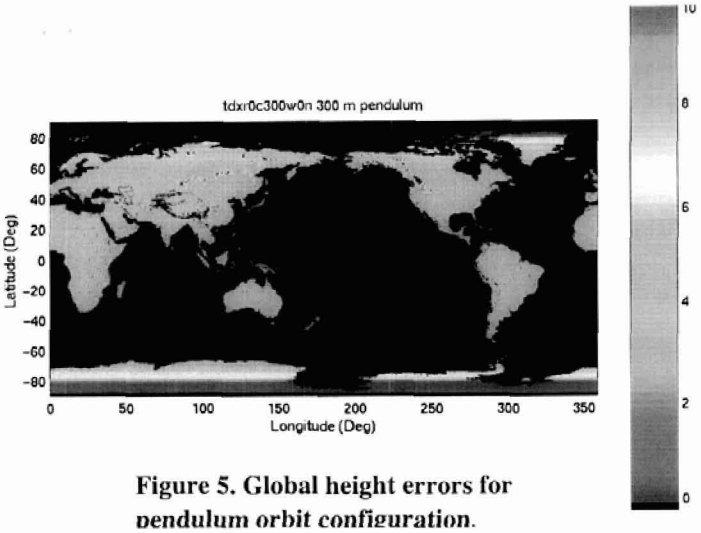

Figure 5. Global height errors for pendulum orbit configuration.

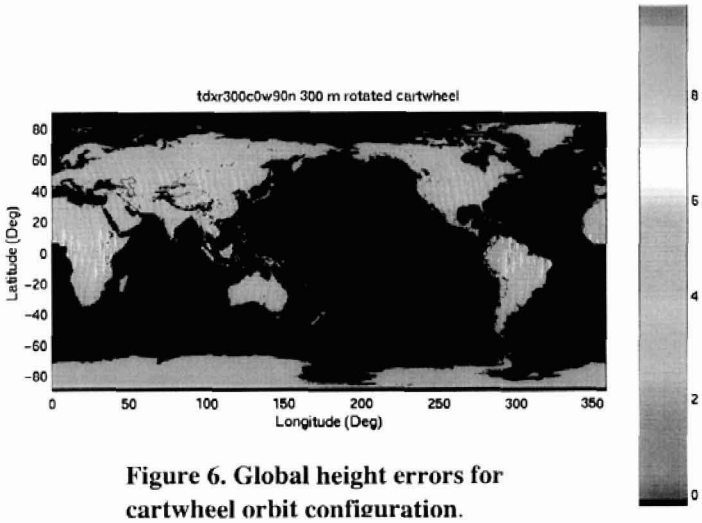

Figure 6. Global height errors for cartwheel orbit configuration.

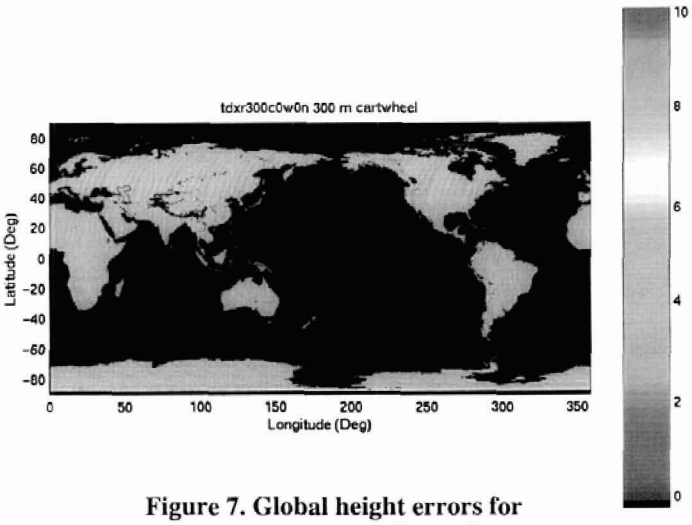

Figure 7. Global height errors for rotated cartwheel configuration.

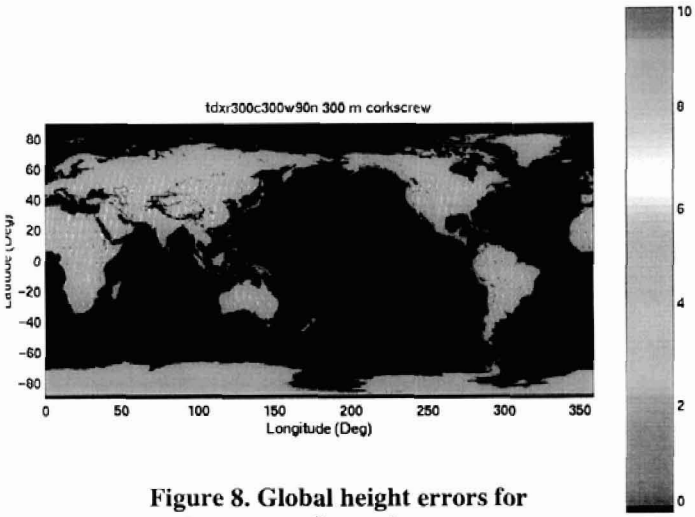

Figure 8. Global height errors for corkscrew configuration.

error source	15% of max CE90(m)	15% of max LE90 (m)	Median CE90 (m)	median LE90 (m)	85% of max CE90 (m)	85% of max LE90 (m)
random phase noise	2.607	1.565	2.775	1.675	2.886	2.194
systematic phase	3.944	2.366	4.210	2.540	4.194	3.186
baseline length	5.174	3.104	5.616	3.390	5.640	4.286
baseline orientation	3.550	2.129	3.648	2.201	3.563	2.708
velocity	0.000	0.000	0.000	0.000	0.000	0.000
wavelength	0.003	0.002	0.005	0.002	0.005	0.003
range	0.083	0.163	0.083	0.163	0.098	0.153
absolute	0.214	0.164	0.214	0.164	0.214	0.164
TOTAL	7.859	4.719	8.386	5.064	8.395	6.381

Table 3. Breakdown of the error components for 3 sample points from the corkscrew orbit configuration. The postings are to 12 meters. DTED Level 3 CE90 (horizontal), LE90 (vertical) relative error requirement is 3, 2 meters respectively. The absolute requirement is 10 meters for both CE90 and LE90. In this study, only random phase noise is considered to contribute to the relative errors.

Appendix

We construct an orthogonal triad

$$\hat{v}, \hat{\beta} = \frac{\hat{b} - (\hat{b} \cdot \hat{v})\hat{v}}{\left|\hat{b} - (\hat{b} \cdot \hat{v})\hat{v}\right|}, \hat{\gamma} = \hat{v} \times \hat{\beta} \text{ as in Figure A1.}$$

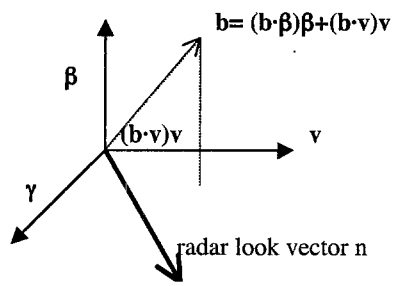

Figure 1. Baseline vector b in the plane β and v

We express the look vector $\hat{n}$ as a composite of the orthogonal axes in (A1) and its variation in (A2).

$$\hat{n} = (\hat{n} \cdot \hat{v})\hat{v} + (\hat{n} \cdot \hat{\beta})\hat{\beta} + (\hat{n} \cdot \hat{\gamma})\hat{\gamma} \qquad \text{(A1)}$$

$$\delta\hat{n} = (\delta\hat{n} \cdot \hat{v})\hat{v} + (\delta\hat{n} \cdot \hat{\beta})\hat{\beta} + (\delta\hat{n} \cdot \hat{\gamma})\hat{\gamma} \qquad \text{(A2)}$$

Processing to constant Doppler $\hat{n} \cdot \hat{v}(Vk / \pi)$ where V is the velocity and k is the wave number $2\pi / \lambda$, requires that $\delta\hat{n} \cdot \hat{v} + \hat{n} \cdot \delta\hat{v} = 0$. First we consider no variation in $\delta\hat{v}$, so that $\delta\hat{n} \cdot \hat{v} = 0$ and since $\hat{n}$ is a unit vector, $\delta\hat{n} \cdot \hat{n} = 0$, we isolate $\delta\hat{n} \cdot \hat{\gamma}$ in (A2) as:

$$(\delta\hat{n} \cdot \hat{\gamma}) = \frac{-(\delta\hat{n} \cdot \hat{\beta})(\hat{\beta} \cdot \hat{n})}{\hat{\gamma} \cdot \hat{n}} \qquad \text{(A3)}$$

Substituting (A3) into (A2) yields (A4).

$$\delta\hat{n} = \left[(\hat{\gamma} \cdot \hat{n})\hat{\beta} - (\hat{\beta} \cdot \hat{n})\hat{\gamma}\right](\delta\hat{n} \cdot \hat{\beta}) \Big/ (\hat{\gamma} \cdot \hat{n}) \qquad \text{(A4)}$$

From (A1) and Figure 1, the [ ] of (A4) is $\hat{n} \times \hat{v}$, which leads to (A5).

$$\delta\hat{n} = \left[\hat{n} \times \hat{v}\right](\delta\hat{n} \cdot \hat{\beta}) \Big/ (\hat{\gamma} \cdot \hat{n}) \qquad \text{(A5)}$$

The interferometric phase ϕ is represented by (A6) where B is the length of the interferometric baseline and variations of this yield (A7).

$$\hat{n} \cdot \hat{b} = -\phi / Bk \qquad \text{(A6)}$$

$$\delta\hat{n} \cdot \hat{b} = -\delta\phi/Bk - \hat{n}\delta\hat{b} \qquad \text{(A7)}$$

Using $\delta\hat{n} \cdot \hat{v} = 0$, it can be shown that $\delta\hat{n} \cdot \hat{\beta}$ (A5) is $\delta\hat{n} \cdot \hat{b} / \hat{\beta} \cdot \hat{b}$, and using (A7), (A5) becomes (A8).

$$\delta\hat{n} = \frac{-(\delta\phi / Bk + \hat{n} \cdot \delta\hat{b})[\hat{n} \times \hat{v}]}{(\hat{\beta} \cdot \hat{b})(\hat{\gamma} \cdot \hat{n})} \qquad \text{(A8)}$$

Finally, $\hat{\gamma} \cdot \hat{n}$ in (A8), which can be expressed as $(\hat{v} \times \hat{\beta}) \cdot \hat{n}$, can be shown to be $\hat{b} \cdot (\hat{n} \times \hat{v}) / \hat{\beta} \cdot \hat{b}$ giving us the final result (A9).

$$\delta\hat{n} = \frac{-(\delta\phi / Bk + \hat{n} \cdot \delta\hat{b})[\hat{n} \times \hat{v}]}{\hat{b} \cdot (\hat{n} \times \hat{v})} \qquad \text{(A9)}$$

In a similar fashion, if we consider variations in $\delta\hat{v} \neq 0$, the variation of the look vector with respect to variations in velocity $\hat{v}$ can be expressed as (A10).

$$\delta\hat{n} = \frac{-(\hat{n} \cdot \delta\hat{v})(\hat{n} \times \hat{b})}{\hat{v} \cdot (\hat{n} \times \hat{b})} \qquad \text{(A10)}$$

Here we started with (A2) and again use $\delta\hat{n} \cdot \hat{n} = 0$, but this time $\delta\hat{n} \cdot \hat{v} = -\hat{n} \cdot \delta\hat{v} \neq 0$. As a first step we again isolate $\delta\hat{n} \cdot \hat{\gamma}$ in (A2) as (A11).

$$\delta\hat{n} \cdot \hat{\gamma} = [(\hat{n} \cdot \delta\hat{v})(\hat{v} \cdot \hat{n}) - (\delta\hat{n} \cdot \hat{\beta})(\hat{\beta} \cdot \hat{n})] / (\hat{\gamma} \cdot \hat{n}) \qquad \text{(A11)}$$

We then substitute (A11) into (A2) and along with (A12) yields (A13).

$$\delta\hat{n} \cdot \hat{\beta} = (\hat{v} \cdot \hat{b})(\hat{n} \cdot \delta\hat{v}) / (\hat{\beta} \cdot \hat{b}) \qquad \text{(A12)}$$

$$\delta\hat{n} = \frac{(\hat{n} \cdot \delta\hat{v})}{(\hat{\gamma} \cdot \hat{n})(\hat{\beta} \cdot \hat{b})}\Big[-(\hat{\beta} \cdot \hat{b})(\hat{n} \cdot \hat{\gamma})\hat{v} + (\hat{v} \cdot \hat{b})(\hat{n} \cdot \hat{\gamma})\hat{\beta} + (\hat{\beta} \cdot \hat{b})(\hat{n} \cdot \hat{v})\hat{\gamma} - (\hat{v} \cdot \hat{b})(\hat{\beta} \cdot \hat{n})\hat{\gamma}\Big] \qquad \text{(A13)}$$

It can then be shown that (A13) is equivalent to (A10).

Acknowledgments

The work described in this paper was carried out at the Jet Propulsion Laboratory, California Institute of Technology, under contract with the National Aeronautics and Space Administration.

References

1. Moreira, Alberto, Gerhard Krieger, Irena Hajnsek, David Hounam, Marian Werner, TanDEM-X: A TerraSAR-X Add-On Satellite for Single-Pass SAR Interferonmetry, IGARSS, 2004.

2. Zebker, H. A., C. L. Werner, P. Rosen, and S. Hensley, Accuracy of topographic maps derived from ERS-1 radar interferometry, IEEE Transactions on Geoscience and Remote Sensing, Vol. 32, No. 4, pp 823-836, July 1994.

3. Paul Rosen, Scott Hensley, Ian R Joughin, Fuk K Li, Søren Madsen, Ernesto Rodríguez, and Richard Goldstein. Synthetic aperture radar interferometry. Proceedings of the IEEE, 88(3), pp 333-382, March 2000.

4. Remco Kroes, Montenbruck, O., Visser P., Precise Grace baseline determintation using GPS, GPS Solutions, Volume 9, Number 1, April 2005.

I would like a clearance and copyright form for my paper for the 2006 IEEE Radar Conference. Attached are my paper, the 1330 form, and the copyright form from the conference.

My group supervisor, Simon Yueh, and my section manager, Soren Madsen, have already reviewed and approved the paper.

I would appreciate your prompt response. The deadline is Thursday February 9.